Structural analysis of shearing mirror assembly in a lateral double-shearing interferometer

ANHU LI[1, 2*], ZHU LUAN[2], XUCHUN JIANG[1], YONGMING BIAN[1], LIJUAN WANG[2], LIREN LIU[2]

[1]College of Mechanical Engineering, Tongji University, No. 4800 Caoan Road, Shanghai, P.R. China

[2]Shanghai Institute of Optics and Fine Mechanics, Chinese Academy of Sciences, P.R. China

*Corresponding author: yfliah@yahoo.com.cn

By the finite element analysis method, the deformation and stress of the double-shearing mirror assembly is studied to validate the feasibility of the opto-mechanical structure. The side axial deformations (within ∅400 mm) of the upper semicircular mirror and the lower one are both up to micrometer order along the *Y*-direction under gravitational action. The equivalent stresses of two semicircular mirrors are more concentrated in the contact areas, but far less than the admissible stress of K9 material. The axial deformations of double-shearing mirror surfaces induced by the temperature rise are very serious, which are the major error sources for the measurement accuracy. The experimental results further validate the analysis conclusions available and show the opto-mechanical design to be reasonable.

Keywords: double-shearing mirror, gravitational action, thermoelastic deformation, finite element analysis, shearing interferometer.

1. Introduction

It is necessary to test and verify the diffraction-limited laser wavefront from a laser communication on the ground before it is used in the space, so some high-accuracy testing equipment must be developed as reference to previous studies [1]. In general, the shearing interferometer has been used as an available interferometry tool for this test [2]. The main types of shearing interferometers include lateral shearing interferometer, radial shearing interferometer, rotation shearing interferometer, and reverse shearing interferometer [3], which all possess some outstanding advantages, such as elimination of the need for a standard reference wave, and simplification of the structure design with stability [4–6]. However, their common weakness is the difficulty of interpreting the shearing interference patterns, which limits the improvement of the measurement accuracy.

In order to increase the sensitivity of the interferometry, we propose a sensitive double-shearing interferometer according to the Jamin interference principle with the horizontal stripe offset in the background [7]. When the input wavefront is close to the diffraction limit, the tilting angle of the upper semicircular mirror and the lower

one will result in the stripe movements towards the opposite direction. As a result, the stripes are increased in one half of the visual field and reduced in the other. Comparing the interference stripes in two half-fields, it can not only improve the minimum detectable wavefront with a higher detection sensitivity, but also make the visual measurement [1, 7]. The creative use of double-shearing mirror component is the key for the double-shearing interferometry, which is arranged by a pair of semicircular wedge-shaped mirrors up and down [8]. Undoubtedly, the integrated analysis of the double-shearing mirror assembly must be carried out to validate its design requirements.

In general, for a large interferometer mirror, in addition to the processing errors, the assembly errors and the adjustment errors, the final quality mainly relates to the two factors: self-weight deformation and thermal deformation [9]. The self-weight deformation is induced by the self-weight of the interferometer mirror and the hold force from the supports. The thermal deformation will occur when a variety of thermal sources act on the mirror located in a thermal environment.

In the past years, the finite element method for the opto-mechanical analysis in an optical interferometer has been used by many researchers [10–15] which can be divided into the following situations: *i*) the mirror shape and different diameter; *ii*) the different supports; *iii*) the different imposition of loads. However, the above three factors have usually been synthesized in many analysis cases. Bigelow introduced the two common radial supports: point support and strap support, the analytical results of which are achieved and compared with the experimental results [15]. Schwesinger and Malvick presented the deformation cases of a variety of large mirrors with different supports under the weight load [11–13]. Cho and Poczulp studied the deformation of the large-scale mirror induced by the temperature change but only considering the temperature gradient [14].

However, the ways of support for the different mirrors discussed in the above references mainly focused on the optical component analysis, and few of them involved the systematic study for the assembly. In practice, the actual deformation generally results from two factors of the primary mirror weight and the supports [10]. More reliable analysis results will be obtained if the assembly analysis can be effectively carried out. In this paper, the finite element analysis for the upper and lower shearing mirror assembly is performed, and the corresponding surface deformation and stress distribution, as well as the PV (peak to valley) values and the RMS (root mean square) values of the wave aberration, are obtained and estimated. Finally, the experimental results of the optical component test further verify the structure design to be reasonable and feasible.

2. Architecture of the system components

2.1. Double-shearing interferometer layout

As shown in Fig. 1, the lateral double-shearing interferometer principle originates from Jamin interferometry with the background horizontal stripe offset [16]. Beam 1 and
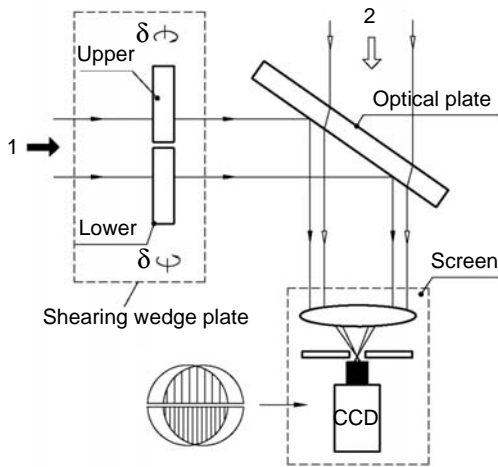
Fig. 1. The principle of the lateral double-
-shearing interferometer.

beam 2 are two interference light beams divided by a beam splitter (omitted in Fig. 1), both of which are generated from the same light source. When the input wavefront is close to the diffraction limit, the respective rotation angle δ of the upper shearing mirror and lower one in the opposite direction will cause displacement of the upper stripes and the lower ones towards the opposite direction [7, 8]. As a result, in the upper half visual field the stripes are reduced while the lower ones are increased correspondingly [8]. Due to the system error elimination through the fringe difference judgement between two half visual fields, this method can improve the measurement accuracy for the wavefront, as well as the detection sensitivity of the minimum detectable wavefront. So it can meet the test requirements of the diffraction-limited wavefront [1, 7].

Figure 2 shows the layout of the upper half wedge-shaped shearing mirror and the lower one. The mirror, 490 mm in diameter and 70 mm in thickness, is adopted
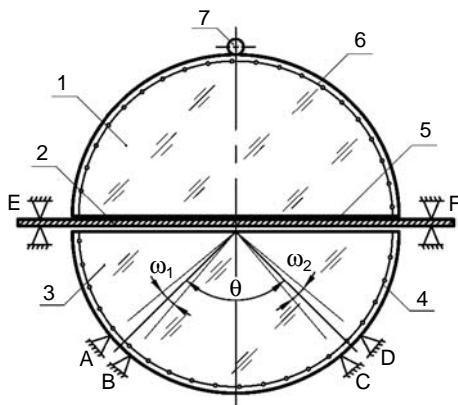

Fig. 2. Double-shearing mirror layout (1 – upper semicircular mirror, 2 – steel plate, 3 – lower semicircular mirror, 4 – ring support for lower semicircular mirror, 5 – wooded board, 6 – ring support for upper semicircular mirror, 7 – point support constraint).

T a b l e 1. Material properties

Material	Density ρ [kg/m^3]	Elastic model E [Pa]	Poisson ratio v	Linear expansion coefficient α	Thermal conductivity D [W m^{-1} °C^{-1}]
K9	2530	8.132×10^{10}	0.209	7.5×10^{-6}	1.207
20 steel	7800	1.98×10^{11}	0.29	11×10^{-6}	48
Wood	470	1.23×10^{10}	0.45	0.8×10^{-6}	0.1

with K9 material, which is divided to two halves along the principal cross-section (namely the upper semicircular mirror and the lower one). The bottom surface of the upper semicircular mirror is supported by a flat steel plate fixed at two ends, and a wooded board is embedded between the steel plate and the mirror. The bottom surfaces of the upper half mirror, wooded board and steel plate are connected with surface-to-surface contact means. So the weight of the mirror and the wooded board is borne by the steel plate. The bottom surface of the lower semicircular mirror is supported by four-point supports of A, B, C and D, which are distributed as two-group layout with $\theta = 90°$ and $\omega_1 = \omega_2 = 10°$. Both lateral planes of the upper semicircular mirror and the lower one are restrained in the ring axial direction, and the optical axis is horizontal. The precision screw adjusters steered by a handwheel are adopted to tilt the upper and lower mirrors. Both the upper part and lower one can be adjusted to change the azimuth and pitch angle by rotating four handwheels [8]. In order to improve the adjustment precision, the arrangement of four precision PZT linear step actuators (piezoelectric ceramic) are coupled with the screw adjusters to compensate the angle adjustment errors, which can also be used as the fine rotation shifter modulators according to the usage requirements. After the whole optical components are set up, they are calibrated to eliminate the original errors by a set of calibrated equipment including a collimated laser source, a collimator, two penta-prims, an alignment plate and so on [8]. The material of steel plate is 20 steel, the width 70 mm, length 710 mm and thickness 3 mm. The width of wooded board is 70 mm, the length 490 mm and the thickness 1 mm. Table 1 shows the material properties of three components.

2.2. Finite element models

Here, a multi-point constrained model is adopted by Ansys software tool to solve the nonlinear contact problem in the contact areas among the steel, the wooded board and the mirror. The contact pressure between the steel plate and the wooded board can be expressed as follows

$$p = \frac{G}{2rh} \tag{1}$$

where p is the uniform pressure, G is the assembly weight, r and h are the radius and the thickness of the mirror, respectively.

The finite element models of the upper and lower mirrors both ignore the small wedge angle (equal to 10″). In order to simplify calculated data, only the 1/2 finite
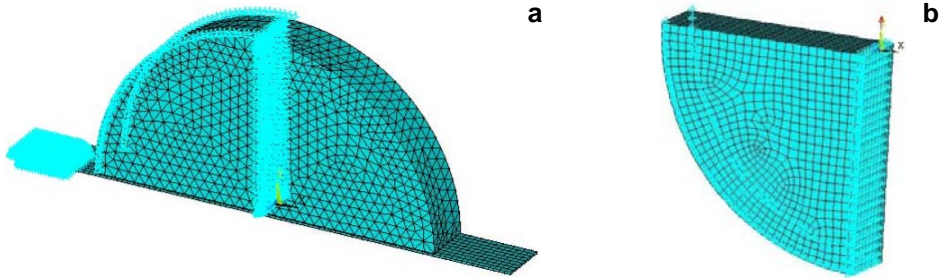
Fig. 3. The finite element model: the upper semicircular mirror (symmetric extension mode) – **a**; the lower semicircular mirror (1/2 model) – **b**.

element models are built by Ansys9.0 with free mesh generation. The primary mirror, the steel plate and the wooded board are all meshed by the solid element (solid95), generating unit numbers 7635 and node numbers 11820, unit numbers 405 and node numbers 3108, and unit numbers 174 and node numbers 1387, respectively. By the constraint equations of surface-to-surface contact, the solid-to-solid model assembly is created. Both ends of the steel plate are constrained by the fixed mounts, and two sides of the mirror are constrained along the ring axial direction. The gravitational acceleration of 9.8 m/s² is exerted on the model and the symmetry constraints are imposed on the symmetry plane. The extended finite element model is shown in Fig. 3**a**.

Figure 3**b** shows the finite element model of the lower semicircular mirror. Considering the structure symmetry, the 1/2 finite element model is built, which is freely meshed by solid95 with a total unit numbers 4640 and node numbers 5634. Two point radial constraints (50° and 40°) are imposed in the axial symmetry plane. The axial displacement constraints are applied to the ring edge, the gravity acceleration of 9.8 m/s² is imposed on the whole model, and the symmetrical constraints are imposed in the 1/2 symmetry plane.

In Figure 3**b**, the contact stress can be calculated according to the Hertz contact theory. Under the load *P* action, a circular spot with a contact circle radius *a* occurs in the point contact area [17],

$$a = \left(\frac{3PR}{4E}\right)^{1/3} = 0.909\left(\frac{PR}{E}\right)^{1/3} \tag{2}$$

Maximum contact pressure p_0 can be expressed as follows

$$p_0 = \frac{3P}{2\pi a^2} = \left(\frac{6PE}{\pi^3 R^2}\right)^{1/3} = 0.578\left(\frac{PE}{R^2}\right)^{1/3} \tag{3}$$

In formulae (2) and (3), *P* is the load acting on the two contact bodies. E_1 and E_2 are respectively the elastic moduli of two cylindrical bodies. Suppose $1/E = (1 - v_1^2)/E_1 + (1 - v_2^2)/E_2$, *E* is the integrated elastic modulus; v_1 and v_2 are

the Poisson's ratios of two-cylinder body material, respectively. R_1 and R_2 are respectively the radii of curvature of two cylinders in the initial contact line, and $R = R_1 R_2 / (R_1 + R_2)$, R is defined as the integrated curvature radius.

3. Results of the shearing mirror analysis

3.1. Results of the assembly analysis

Figure 4**a** shows the results of analysis of the whole assembly. The deformation mainly concentrates in the load-bearing areas of the steel plate, and the transition deformation is between the fixed ends of the steel plate and the contact area of the mirror. The maximum deformation is 23.7 µm. When the spacing of the two fixed ends is adjusted, the assembly deformation varies significantly, which shows the deformation induced by the layout of fixed constraints is very serious. The *Y*-direction, namely the gravity action direction, represents the main deformation trend. The deformation along the *X*- and *Z*-direction is relatively small, mainly occurring between the steel plate side and the contact area.
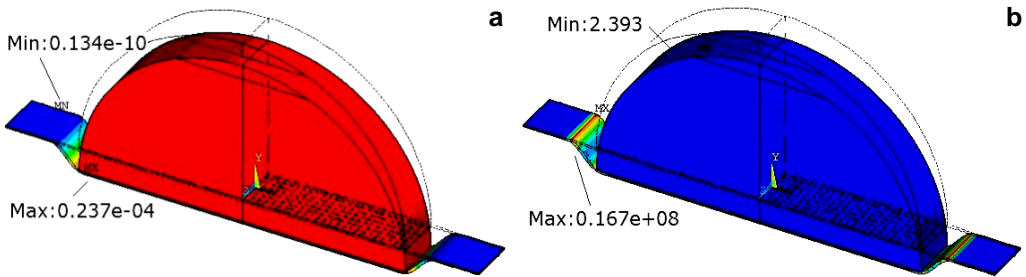

Fig. 4. Results of analysis of the upper semicircle shearing mirror assembly deformation contour (**a**), equivalent stress contour (**b**).

Figure 4**b** gives the equivalent stress of the assembly, near 16.7 MPa, mainly occurring in two fixed ends of the steel plate. Table 2 lists the analysis results of the deformation and stress in the assembly exposed to the gravitational action.

3.2. Results of analysis of the components

The upper semicircular mirror assembly includes the support steel plate, the wooded board and the mirror, which can be extracted to study respectively. The steel plate is

T a b l e 2. The deformation and stress of the assembly structure.

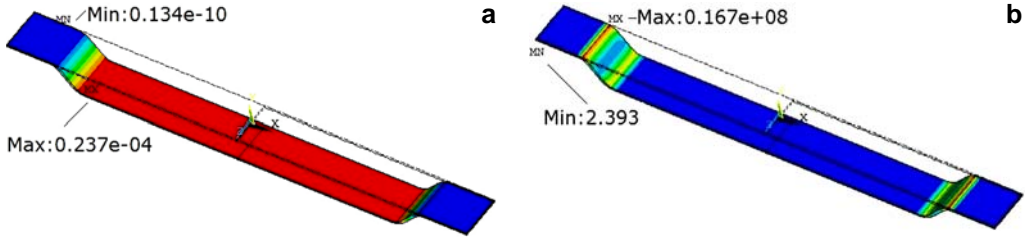|	*X*		*Y*		*Z*		Total	
	Max	Min	Max	Min	Max	Min	Max	Min
Deformation [µm]	1.09	−1.13	2.63	−23.7	2.80	−2.81	23.7	0.13×10^{-4}
Equivalent stress [MPa]	17.6	−17.9	1.16	−1.52	5.28	−5.33	16.7	2.93×10^{-6}

Fig. 5. Results of analysis of the steel plate deformation cloud (**a**), equivalent stress (von Mises stress) (**b**).

the bearing component, both ends of which are constrained and the middle part bears the uniform pressure. Figure 5**a** shows the deformation of the steel plate. The maximum deformation is 23.7 μm mainly occurring in the overall contact area, and the minimum deformation occurs in two fixed ends. The transition deformation area is between two fixed ends and the contact area. The main deformation is along the *Y*-direction. The deformation values along the *X*- and *Z*-direction are both less, near sub-micrometer order, which can be ignored to simplify the analysis process.

Figure 5**b** shows the equivalent stress of the steel plate. The maximum stress is 16.7 MPa and mainly occurs in the transition region between two fixed ends and the contact area, far less than the allowable stress of 20 steel, $[\sigma] = 325$ MPa (20 steel). The stress along the *X*-direction is near to 10 MPa, which relates to the tensile load action of the steel plate, but the stress along the *Y*-direction and the *Z*-direction is of megapascal magnitude. The overall stress distribution in the assembly structure is within the admissible stress range of each material. Table 3 gives the deformation and stress details of the steel plate and the wooded board.

Figure 6**a** shows the overall displacement of the bearing wooded board in the middle position. Compared to the original position (shown by the dotted line), the maximum displacement is 23.6 μm mainly along the *Y*-direction, and the minimum displacement is 22.8 μm, but the wooded shape almost does not change. However, the displacement of the wooded board is determined by the steel plate position, so it will not actively affect the displacement of the assembly structure.

Figure 6**b** gives the equivalent stress analysis results of the wooded board. The maximum equivalent stress is 1.9 MPa and the minimum stress is about 2100 Pa, which is far less than the allowable stress of the wooded board, $[\sigma] = 7$ MPa. The stress

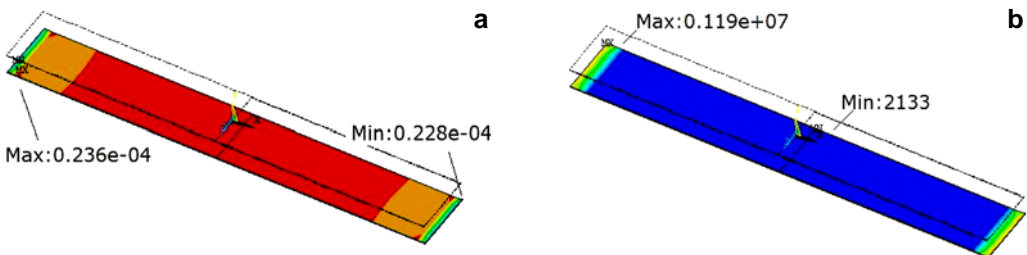Fig. 6. Results of analysis of the wooded board deformation (**a**), equivalent stress (von Mises stress) (**b**).

T a b l e 3. The deformation (µm) and equivalent stress (MPa) of the steel plate and the wooded board.

Component	Items	X		Y		Z	
		Max	Min	Max	Min	Max	Min
Steel plate	Deformation	1.09	–1.13	2.63	–23.7	0.12	–0.123
	Stress	17.6	–17.9	1.16	–1.14	5.28	–5.33
Wooded board	Deformation	0.11	–0.18	–22.8	–23.6	0.28	–0.28
	Stress	0.19	0.23	0.65	–1.52	0.29	–0.73

Component	Items	Total	
		Max	Min
Steel plate	Deformation	23.7	0.13×10^{-4}
	Stress	16.7	2.93×10^{-6}
Wooded board	Deformation	23.6	22.8
	Stress	1.19	0.21×10^{-2}

magnitude in the wooded board is sub-MPa along the *X*- and *Z*-direction, but the maximum stress (absolute value) reaches megapascal magnitude along the *Y*-direction. Comparing the stress analysis results in three directions, we can find the stress along *Y*-direction to be more concentrated, but it is still within the admissible range for the structure. Table 3 gives the deformation and stress values of the wooded board.

The mirror is the key component of the system. Its side surface within ∅400 mm is especially taken to be analyzed. The maximum deformation is 23.5 µm, mainly in the central area of the mirror along the *Y*-direction, namely near the symmetry plane, which is the main deformation direction.

In fact, the axial deformation of the mirror surface along the *Z*-direction is the main factor of the wave aberration. The Δ*Z* coordinates can be expressed by the function of the (*X*, *Y*) coordinates, only considering the surface deformation within ∅400 mm. The wave aberration can be expressed as follows

$$W(x, y) = (n - 1)\Delta Z(x, y) \tag{4}$$

where *W* is the wave aberration induced by the axial deformation, including the wave aberration of PV and RMS, and *n* is the refractive index.

T a b l e 4. The deformation and stress of the mirror surface within ∅400 mm.

	Equivalent stress [MPa]		Deformation [nm]		PV	RMS
	Max	Min	Max	Min		
Total	0.0221	0.00797	23.5×10^{6}	–	–	–
X-direction	0.141	–0.118	1.22×10^{-2}	-4.82×10^{-2}	–	–
Y-direction	0.0062	–0.0064	-23.5×10^{-2}	–	–	–
Z-direction	0.70×10^{-3}	-0.86×10^{-3}	1.76	–4.21	5.97	0.941

Min: −0.144×10⁻⁹   **a**   Min: 593.553   **b**
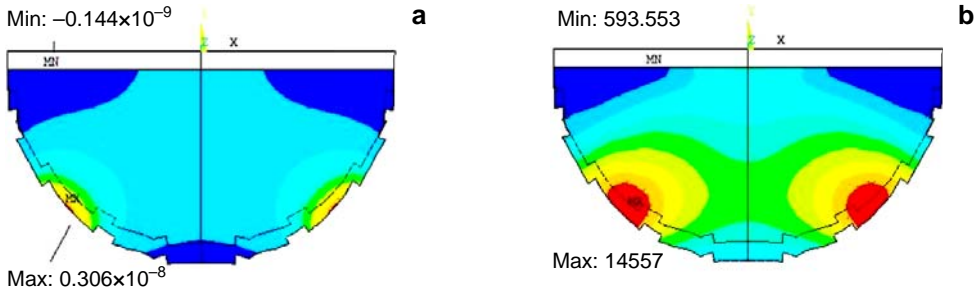

Max: 0.306×10⁻⁸   Max: 14557

Fig. 7. Results of analysis within ∅400 mm axial deformation (**a**), equivalent stress (von Mises stress) (**b**).

As a result, the PV and RMS values are obtained to indicate the shape change, and the maximum and the minimum axial deformation is 4.21 nm and 1.76 nm, respectively. Table 4 shows the analysis results of the deformation and stress in the mirror sides.

3.3. Structural analysis of the lower semicircular shearing mirror

Figure 7 gives the analysis results of the deformation and stress in the lower semicircular mirror under the gravitational action. The maximum deformation is close to micrometer order and the maximum equivalent stress occurs at the support point. Figure 7**a** shows that the maximum axial deformation is 3.06 nm and the minimum axial deformation is –0.140 nm. Figure 7**b** shows that the maximum equivalent stress occurs in the vicinity of the fulcrum. The ΔZ coordinates corresponding to the mirror surface (X, Y) coordinates within ∅400 mm are further studied, and the PV and RMS values are obtained.

4. Thermoelastic deformation analysis

4.1. Thermoelastic deformation of the upper semicircular mirror

The thermoelastic deformation originates from the two factors: temperature and gravity, which is the heat–stress coupling issue. By the sequence analysis method, the thermal analysis is firstly made to solve the column vector of node temperature, which is then submitted to the structural analysis as the physical load, and finally the thermal-structural coupled analysis can be carried out [11, 18].

Here, we only discuss the internal temperature gradient caused by the thermal deformation. The environmental reference temperature is set at $T = 20$ °C, and the internal temperature is 0.05 °C, 0.10 °C, 0.30 °C and 0.50 °C. The maximum deformation of the upper assembly is 25.4 µm and the maximum equivalent stress is 17.9 MPa as the temperature rises to 20.50 °C, mainly occurring in the steel contact area. Table 5 lists the analytical results of the deformation and stress of each substructure and the assembly. Due to the different thermal expansion coefficients of

T a b l e 5. The deformation (μm) and stress (MPa) of the upper semicircular mirror assembly with the temperature changes.

			Temperature changes [°C]			
			0.05	0.10	0.30	0.50
Mirror	Deformation	Max	23.2	23.5	23.8	24.2
		Min	22.1	23.2	22.7	22.1
	Equivalent stress		1.17	1.51	1.67	1.81
Wooded board	Deformation	Max	23.6	23.8	24.4	24.8
		Min	22.8	22.8	22.7	22.7
	Equivalent stress		1.19	1.21	1.30	1.33
Steel plate	Deformation	Max	23.6	23.9	24.5	24.8
		Min	33.6×10^{-4}	68.6×10^{-4}	0.02	0.034
	Equivalent stress		16.8	16.9	17.4	17.9
Assembly	Deformation	Max	23.6	23.8	24.5	25.4
		Min	33.9×10^{-4}	68.6×10^{-4}	0.02	0.034
	Equivalent stress		16.8	16.9	17.4	17.9

the wooded board, the mirror and the steel plate, the deformation of the assembly is towards the *Y*-direction with the free expansion under the thermal effects.

The shape changes of the mirror side are further analyzed within ⌀400 mm. In order to simplify the analysis process, the deformation along the *X*- and *Y*-direction is ignored, only the axial deformation of the mirror surface, namely the *Z*-direction, is considered, which is shown in Fig. 8.

When the temperature rises $\Delta T = 0.020$ °C, the PV and RMS values of the mirror surface are roughly doubles of those under the gravitational action only. When
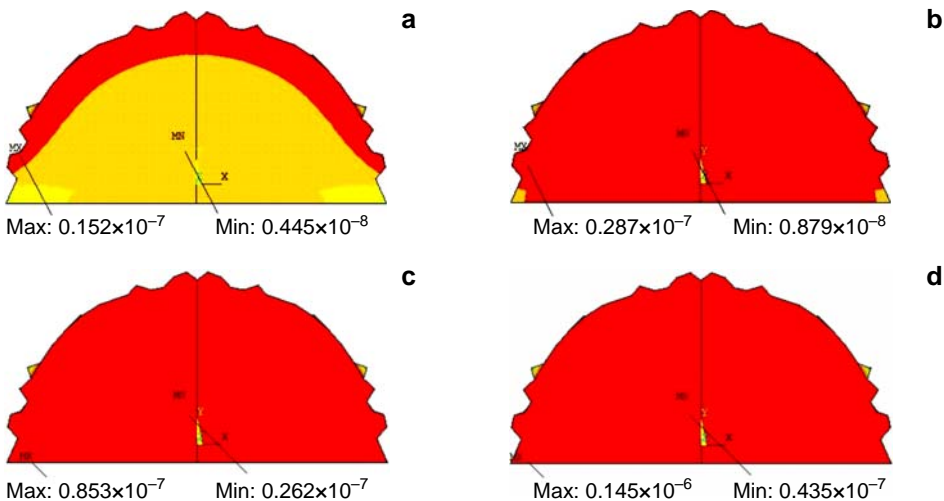

Fig. 8. The side axial deformation with the temperature rise within ⌀400 mm area; 20.05 °C (**a**), 20.1 °C (**b**), 20.3 °C (**c**), 20.5 °C (**d**).

T a b l e 6. The side axial deformation (nm) within ∅400 mm with the temperature changes.

		Temperature changes [°C]			
		0.05	0.10	0.30	0.50
	Max	15.2	28.7	85.3	145
	Min	4.45	8.79	26.2	43.5
Axial deformation	PV	10.8	19.9	59.1	102
	RMS	1.76	2.85	13.8	18.9

the tempera-ture continues to rise $\Delta T = 0.50$ °C, the PV values of wave aberration in the mirror side surface reach $\lambda/6$, close to the Rayleigh criterion, which is very serious. Analysis results of the temperature changes in four temperature intervals further show that the maximum axial deformation starts from the upper part of the mirror in ∅400 mm and the deformation is not obvious due to the overall constraints, which accords to the previous analysis results for the axial deformation of the mirror only under the gravitational action. Table 6 shows the deformation values of the mirror side within ∅400 mm.

As shown in Table 6, when the temperature rises from $\Delta T = 0.02$ °C to $\Delta T = 0.50$ °C, the axial deformation increases with the temperature rise according to a linear relationship. When the temperature increases $\Delta T = 0.50$ °C, the maximum axial deformation in the mirror side is up to sub-micrometer, so the thermal effect on the instrument performance is very serious.

4.2. Thermoelastic deformation of the lower semicircular mirror

The reference environmental temperature is also set at $T = 20$ °C, the internal temperature is 0.05 °C, 0.10 °C, 0.30 °C and 0.50 °C. Figure 9 visually gives the mir-
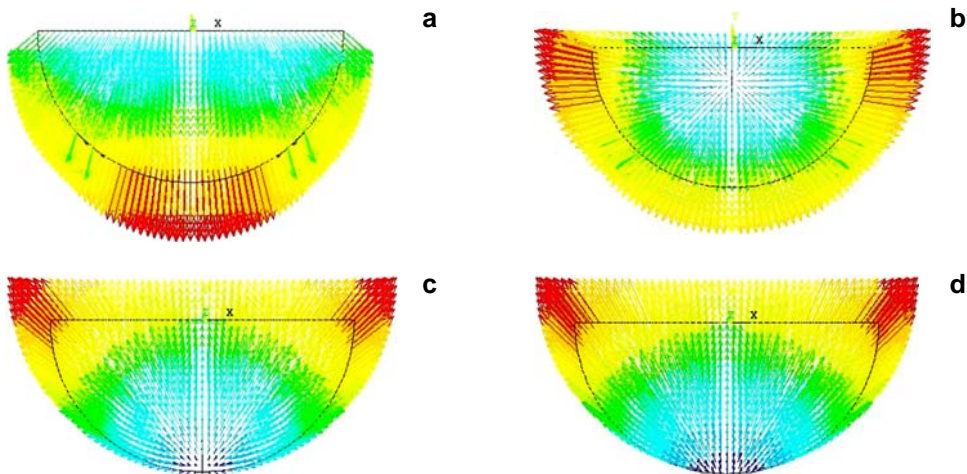

Fig. 9. The thermoelastic deformation vector; $T = 20.05$ °C (**a**), $T = 20.1$ °C (**b**), $T = 20.3$ °C (**c**), T = 20.5 °C (**d**).
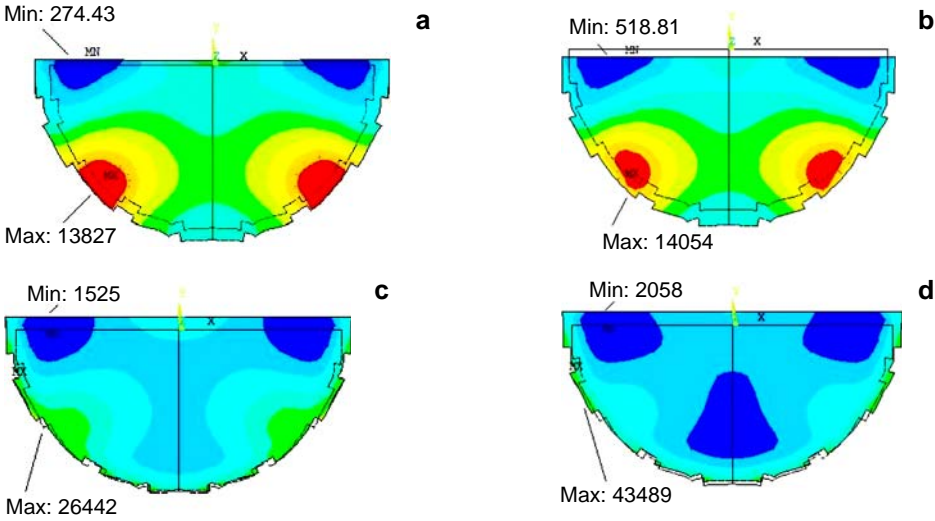
Fig. 10. The relationship between the equivalent stress and the temperature changes within ⌀400 mm in the mirror side along the optical axis direction; $T = 20.05$ °C (**a**), $T = 20.1$ °C (**b**), $T = 20.3$ °C (**c**), $T = 20.5$ °C (**d**).

ror deformation vector with the temperature change. The free expansion of the mirror is basically along the *Y*-direction under the heat loads. Especially, the mirror side in ⌀400 mm is studied for the analysis of shape changes. Figure 10 gives the equivalent stress distribution within ⌀400 mm.

When the temperature rises $\Delta T = 0.02$ °C, the PV values and RMS values of mirror surface in ⌀400 mm show roughly a many fold increase. As the temperature continues to increase $\Delta T = 0.50$ °C, the PV values of the surface in the mirror side reached $\lambda/6$, close to the Rayleigh criterion. The analysis results of four temperature intervals further show that the maximum thermoelastic stress caused by the temperature change starts from the fulcrum of the mirror, which agrees with the previous analysis results

T a b l e 7. The axial deformation (nm) and equivalent stress (MPa) with the temperature change in ⌀400 mm.

		Temperature changes [°C]			
		0.05	0.10	0.30	0.50
Axial deformation	Max	−9.82	29.8	83.3	138
	Min	−16.4	19.7	59.3	98.6
	PV	6.58	10.1	24	39.4
	RMS	1.04	1.51	4.07	5.63
Equivalent stress	Max	0.0138	0.0140	0.0264	0.0435
	Min	0.274×10^{-3}	0.518×10^{-3}	0.0015	0.0021

only considering the gravitational action. Table 7 shows the analysis results of the axial deformation and the equivalent stress within the side surface in $\varnothing$400 mm.

5. Conclusions

The lateral double-shearing interferometer can meet the requirements of high-accuracy wavefront measurement through the adjustments of the double-shearing mirror, including an upper semicircular mirror and a lower one. The upper part adopts the composite supports of a steel plate and a wooded board together with radial constraints, and the lower part is supported by four floating points. In this paper, according to the optimal design results, the finite element method is used to analyze the deformation and stress of the shearing mirror assembly under the gravitational action and the thermal effects.

The maximum axial deformation of the upper semicircular mirror is close to micrometer magnitude along the *Y*-direction under the gravitational action, which is the major error factor that affects the interferometric accuracy. The maximum deformation of the steel plate and the wooded board is of micrometer order. The maximum equivalent stresses of various components in the assembly are all less than the corresponding admissible stress of each material. The deformation in the lower semicircular mirror is along the *Y*-direction under the gravitational action, and the stress in the floating-point support is more concentrated, but far less than the K9 admissible stress. The axial deformation within $\varnothing$400 mm is nanoscale, much less than the Rayleigh criterion.

The deformation and the stress with temperature changes in the upper semicircular mirror and the lower one are studied accordingly. The surface axial deformation induced by the temperature rise is very serious. In a small range of temperature fluctuation, the deformation is basically proportional to the temperature rise. When the temperature rises to 0.5 °C, the deformation value is close to the Rayleigh criterion. Moreover, the stress changes induced by the temperature fluctuation are also very serious. So the opto-mechanical design is needed to consider the temperature effects. Two methods have been adopted to avoid the thermal effects. During the design process we permit the possible deformations of both the upper half mirror and the lower one freely towards the *Y*-direction, but the optical axis is always horizontal [8]. Meanwhile the whole testbed is always located in a temperature-controlled laboratory where the temperature fluctuates less than 0.5 °C. Therefore, the circumstance temperature basically keeps constant and has less effect on the application of the instrument.

However, in the above analysis process, the analytical models are simplified, which especially concerns the lower mirror supported by rigid supports. But, in fact, the supports for large optical components generally are elastic, and therefore the stress and strain responses ought to be less than some of the above analysis. We adopt a Zygo Mark interferometer to measure the PV and RMS values of the upper and lower

mirror assemblies with elastic supports under the temperature of 20 °C and 20.5 °C in a temperature-controlled laboratory. The measured PV and RMS values under the temperature 20.5 °C are nearly nine times larger than those under the temperature of 20 °C, which are less than the value of theoretical calculation with about 15% error. So, we can conclude that the above analysis is valid. Compared with the test results for a normal optical plate by a large aperture phase-shifter interferometer (accuracy up to 0.02λ), their experimental results well agree with each other. Therefore, we can conclude that the instrument can meet the design requirements. This shearing interferometer can be used not only to detect the wavefront error in the laser communication field, but also to calibrate other high-precision optical components and equipment.

References

[1] LIU L.R., WANG L.J., LUAN Z., SUN J.F., LI A.H., LIU D.A., *Physical basis and corresponding instruments for PAT performance testing of inter-satellite laser communication terminals*, Proceedings of SPIE **6304**, 2006, pp. 63040C1–6304C11.

[2] SIROHI R.S., KOTHIYAL M.P., *Double wedge plate shearing interferometer for collimation test*, Applied Optics **26**(19), 1987, pp. 4054–4056.

[3] BORN M., WOLF E., *Principles of Optics*, Cambridge University Press, Cambridge, 1999, pp. 302–308.

[4] XU R.W., LIU H.Z., LUAN Z., LIU L.R., *A phase-shifting vectorial-shearing interferometer with wedge plate phase-shifter*, Journal of Optics A: Pure Applied Optics **7**(11), 2005, pp. 617–623.

[5] LUAN Z., LIU L.R., LIU D.A., TENG S.Y., *Jamin double-shearing interferometer for diffraction--limited wave-front test*, Applied Optics **43**(9), 2004, pp. 1819–1824.

[6] LEE Y.W., CHO H.M., LEE I.W., *Half-aperture shearing interferometer for collimation testing*, Optical Engineering **32**(11), 1993, pp. 2837–2840.

[7] LUAN Z., LIU L.R., WANG L.J., LIU D.A., *Large-optics white light interferometer for laser wavefront test: Apparatus and application*, Proceedings of SPIE **7091**, 2008, p. 70910Q.

[8] WANG L.J., LIU L.R., LUAN Z., SUN J.F., ZHOU Y., LIU D.A., *The mechanical design of the large--optics double-shearing interferometer for the test of the diffraction-limited wavefront*, Proceedings of SPIE **7091**, 2008, p. 70910S.

[9] HATHEWAY A.E., *Mountings for a four meter glass mirror*, Proceedings of SPIE **1303**, 1990, pp. 142–147.

[10] LI A.H., BIAN Y.M., LIANG Y.C., ZHU Y.J., *Integrated design for large-scale opto-mechanical structure*, Optica Applicata **39**(2), 2009, pp. 383–389.

[11] SCHWESINGER G., *Optical effect of flexure in vertically mounted precision mirrors*, Journal of Optical Society of America **44**(5), 1954, pp. 417–424.

[12] MALVICK A.J., *Dynamic relaxation: A general method for determination of elastic deformation of mirrors*, Applied Optics **7**(10), 1968, pp. 2117–2121.

[13] MALVICK A.J., *Theoretical elastic deformations of the Steward Observatory 230-cm and the Science Center 154-cm mirrors*, Applied Optics **11**(3), 1972, pp. 575–585.

[14] Cho M.K., Poczulp G.A., *Surface distortion of a 3. 5-meter mirror subjected to thermal variations*, Proceedings of SPIE **1532**, 1991, pp.137–145.

[15] Bigelow B.C., *Finite element analysis of large lenses for the Keck telescope high resolution echelle spectrograph*, Proceedings of SPIE **1532**, 1991, pp. 15–26.

[16] Wang L.J., Liu L.R., Sun J.F., Zhou Y., Luan Z., Liu D.A., *Method to measure frequency change of tunable laser based on Jamin shearing interferometer*, Proceedings of SPIE **7432**, 2009, p. 743218.

[17] Fischer-Cripps A.C., *Introduction to Contact Mechanics*, 2nd Edition, Springer, 2007.

[18] Person E., Stepp L., *Response of large mirrors to thermal distributions*, Proceedings of SPIE **0748**, 1987, pp. 215–228.